

Synthesis of Ultrathin Zeolite Y Membranes and their Application for Separation of Carbon Dioxide and Nitrogen Gases

Jeremy C. White,[†] Prabir K. Dutta,^{*,†} Krenar Shqau,[‡] and Henk Verweij[‡]

[†]Department of Chemistry, The Ohio State University, 100 West 18th Avenue, Columbus, Ohio 43210, and
[‡]Department of Materials Science and Engineering, The Ohio State University, 2041 College Road, Columbus, Ohio 43210

Received January 31, 2010. Revised Manuscript Received March 24, 2010

Synthesis of zeolite Y membranes from submicrometer (> 100 nm) and nano seed (< 100 nm) crystals on alumina supports was examined and the separation characteristics of these membranes for CO₂ and N₂ were studied. Two secondary growth solutions were examined, one for a rapid growth (hours) and one for a slower growth process (days). Membranes formed from the rapid growth solution resulted in 2–2.5 μ m thickness, while for the slower growth solution, a dense membrane of 350–600 nm thickness was formed, covered by a 25 μ m porous zeolite layer. With the nano seeds as the seeding layer, no membrane was formed. A mechanism involving seed dissolution to initiate membrane formation is concluded. The separation characteristics of membranes for CO₂/N₂ separation were similar, with very high selectivities for separation ($\alpha_{\text{CO}_2/\text{N}_2} > 500$). The thicker membrane had lower permeance. By investigating both single gas and mixed gas permeances, strong evidence for a percolative type separation process is obtained.

Introduction

Supported zeolite films/membranes with controlled microstructures are important in applications as diverse as catalysis, ion-exchange, nuclear waste disposal, light harvesting devices, chemical sensing, and gas separations.^{1–3} Over the past 2 decades, membranes of various zeolite structure types, formed on inorganic porous supports, have shown enormous potential for separations of gas and liquid mixtures. Separation by zeolite membranes are controlled by two factors. The first is size exclusion, in which certain species are discriminated against since they cannot enter into the zeolite pore due to size restrictions. Second, for those molecules that enter into the zeolite pores, membrane transport and separation are dependent upon a combination of affinity (sorption) and mobility (diffusion).^{4–6}

CO₂ separation is one of the most studied applications for zeolite Y membranes because of its industrial significance, such as CO₂ capture for carbon sequestration, natural gas purification, and separation of product streams from water gas shift reactions for hydrogen production.^{7–11} Because of the window size (0.73 nm) of zeolite Y, there is no steric hindrance for molecules, like CO₂, CH₄, CO, H₂O, or N₂, to enter in the pores. However, for

molecules like CO₂, there is preferential interaction with the aluminosilicate framework and the extraframework cations which leads to a favorable combination of sorption and mobility. Thus, with gas mixtures containing CO₂ and N₂ or CH₄, the CO₂ permeates preferentially through the zeolite by surface diffusion, while N₂ (CH₄) is excluded from the faujasite pores due to preferential CO₂ adsorption and pore constriction.^{8,10}

Membrane performance is expressed in terms of the permeance, f_l , of species l , and the intrinsic selectivity, α_{l_1, l_2} , for mixtures of species l_1 and l_2 ; $f_l = j_l/\Delta p_l$ where j is the molar flux and Δp the partial pressure difference of l between the membrane feed, f , and permeate, p , side. $\alpha_{l_1, l_2} = f_{l_1}/f_{l_2}$; l_1 is the *major species* (here CO₂) for which the permeance is expected to be the highest for most conditions. The permeability is defined as $k_l = f_l \times X$, with X being the membrane thickness. The permselectivity is defined as $\alpha_{l_1, l_2}^s = f_{l_1}^s/f_{l_2}^s$, where f^s is obtained in one-component (single) gas measurements. In general, f_l depends on state parameters at the feed and permeate side of the membrane. If all p_l are low so that Henri's sorption law applies, f_l is independent of p_l at low p_l .

The dominant membrane transport mechanism in porous structures depends strongly on the pore size, \emptyset_p . Following IUPAC, we distinguish:¹²

- Microporous structures with $\emptyset_p < 2$ nm, in which gas transport occurs by *molecular hopping diffusion* with strong interaction with the host.
- Mesoporous structures with $2 \text{ nm} < \emptyset_p < 50$ nm, in which gas transport generally occurs by slight selective *Knudsen diffusion*.
- Macro-porous structures with $\emptyset_p > 50$ nm, in which gas transport generally occurs by nonselective *viscous flow*.

Micropore transport of molecules is relevant for this study, and we distinguish two types of phenomena: type I with all molecules present at low concentrations and type II with the major species

*Corresponding author. Telephone: +1 614 2924532. Fax: +1 614 6885402. E-mail: dutta@chemistry.ohio-state.edu.

(1) Dutta, P. K.; Payra, P. In *Handbook of Zeolite Science and Technology*; Auerbach, S. M., Carrado, K. A., Dutta, P. K., Eds.; Marcel Dekker, Inc.: New York, 2003; p 1.

(2) Bernardo, P.; Algieri, C.; Barbieri, G.; Drioli, E. *Desalination* **2006**, *200*, 702.

(3) Kim, Y.; Das, A.; Zhang, H.; Dutta, P. K. *J. Phys. Chem. B* **2005**, *109*, 6929.

(4) Coronas, J.; Noble, R. D.; Falconer, J. L. *Ind. Eng. Chem. Res.* **1998**, *37*, 166.

(5) Flanders, C. L.; Tuan, V. A.; Noble, R. D.; Falconer, J. L. *J. Membr. Sci.* **2000**, *176*, 43.

(6) Gump, C. J.; Noble, R. D.; Falconer, J. L. *Ind. Eng. Chem. Res.* **1999**, *38*, 2775.

(7) Seike, T.; Matsuda, M.; Miyake, M. *J. Mater. Chem.* **2002**, *12*, 366.

(8) Kusakabe, K.; Kuroda, T.; Morooka, S. *J. Membr. Sci.* **1998**, *148*, 13–23.

(9) Hasegawa, Y.; Kusakabe, K.; Morooka, S. *Chem. Eng. Sci.* **2001**, *56*, 4273–4281.

(10) Kusakabe, K.; Kuroda, T.; Uchino, K.; Hasegawa, Y.; Morooka, S. *AIChE J.* **1999**, *45*, 1220.

(11) McLeary, E. E.; Jansen, J. C.; Kapteijn, F. *Microporous Mesoporous Mater.* **2006**, *90*, 198.

(12) Koros, W. J.; Ma, Y. H.; Shimidzu, T. *Pure. Appl. Chem.* **1996**, *68*, 1479.

present at high concentrations in the membrane. For type I, $\alpha_{l_1, l_2}^s \approx \alpha_{l_1, l_2}$ and k_l is independent of X . For type II, α_{l_1, l_2}^s can be much larger than α_{l_1, l_2} ; k_{l_1} is independent of X , while k_{l_2} decreases with X . The latter is due to the percolative nature of transport of l_2 .¹³

Knudsen and viscous flow play an important role in adversely affecting membrane performance:

- The presence of connected meso- or macropore “defects”, which can reduce α , even at low defect concentrations.
- Building up transport resistance in the membrane support structure.

Thus, overall permeance can be increased by reducing membrane and support thickness. However, decreasing the membrane thickness can increase the concentration of membrane defects, while reducing support thickness will decrease strength.

Utilizing NaY-type membranes supported on tubular alumina supports, Kusakabe et al. obtained $\alpha_{\text{CO}_2, \text{N}_2}$ in the range of 20–100 at 303 K for equimolar mixtures, as well as a maximum f_{CO_2} up to 1.5×10^{-6} mol/(m² s Pa).^{8–10,14} Kusakabe et al. also studied the effect of temperature, T , and the extra-framework cations on $\alpha_{\text{CO}_2, \text{N}_2}$. For NaY membranes, $\alpha_{\text{CO}_2, \text{N}_2}$ decreased with temperature and improved when the membranes were ion-exchanged with other alkali cations (Cs⁺, Rb⁺, K⁺).^{8,10,15,16} Other researchers have published similar results for zeolite Y-based separations of CO₂ from N₂.^{7,17–19}

Although significant progress has been made in the synthesis of zeolite Y membranes, issues that still need to be addressed include reproducibility of membrane synthesis, control of defects, and development of ultrathin membranes. Novel strategies have focused on the seeding and secondary growth processes.^{17,20} The influence of chemical composition on the particle size of zeolite Y seed crystals is described in the literature.^{21–24} In this paper, we examine the formation of zeolite Y membranes on alumina supports. With the use of uniformly deposited seed layers of submicrometer zeolite Y crystallites, two hydrothermal secondary growth procedures with different crystal growth rates were examined. Structural and morphological characterization of these membranes was done with X-ray diffraction and electron microscopy. Transport measurements were carried out for CO₂ and N₂ and their mixtures, and the separation properties were correlated with the membrane characteristics. Though there have been reports for synthesis of ultrathin zeolite A and MFI membranes and a permporometry study,^{25,26} the present report is the first to

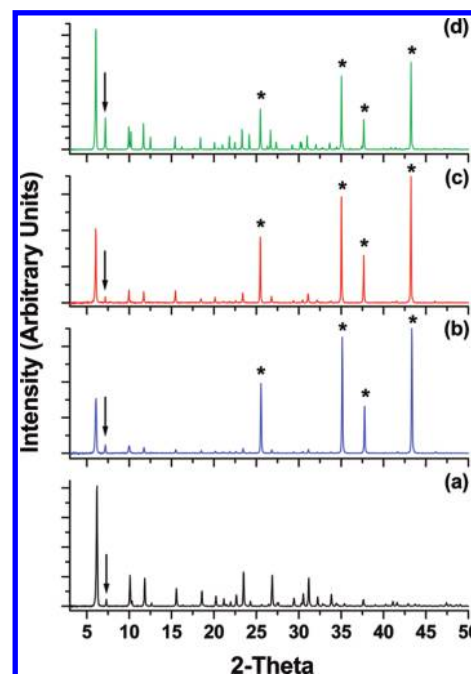


Figure 1. X-ray diffraction patterns of submicrometer zeolite Y membranes prepared using 2 different growth procedures. (a) submicrometer zeolite Y powder, (b) submicrometer zeolite Y seeded support, (c) composition A membrane, (d) composition B membrane. (Zeolite A impurity labeled with arrow; the asterisk indicates alumina support.)

synthesize ultrathin zeolite Y membranes and study their CO₂/N₂ gas separation characteristics.

Results

Membrane Synthesis and Characterization. The powder X-ray diffraction pattern of the calcined, submicrometer seed crystals shown in Figure 1a confirms the formation of zeolite Y, along with a small amount of zeolite A (marked by an arrow) estimated at <5% based on the comparison of the (111) intensities). Besides the zeolite A and the alumina peaks marked by asterisks, all of the other peaks are due to zeolite Y. The crystal size was 80–200 nm, as determined by dynamic light scattering and confirmed by SEM. Stable colloidal suspensions of these crystals could be prepared in the absence of any dispersants or polymers, and were used for dip-coating the macro-porous alumina supports. The XRD pattern of a supported zeolite Y seed layer is shown in Figure 1b (prepared using a 5 mg/mL dipping solution) and the SEM top view is shown in Figure 2a. The higher resolution inset in Figure 2a shows a rather porous, heterogeneous packing morphology within the seed layer. This is ascribed to the polydispersity in zeolite particle size and the presence of zeolite A impurities (of cubic morphology). The SEM cross-section in Figure 2b shows the presence of a ~1.6 μm thick seed layer.

The seed layers were converted into zeolite Y membranes using two growth solutions, which are referred to as composition A or B. These growth solutions were chosen because of the time differences it takes for crystallization to occur, with composition A being about 10 times faster than composition B. Growth was carried out in composition A for 8 h at 363 K. Figure 3a shows a top-view of the resulting membrane, with void spaces between neighboring particles, which indicates that the membrane was not yet continuous. Hence, the membrane was placed in a fresh composition A solution for 8 h more, and the top view of the

(13) Verweij, H. J. *Mater. Sci.* **2003**, *38*, 4677.

(14) Kusakabe, K.; Kuroda, T.; Murata, A.; Morooka, S. *Ind. Eng. Chem. Res.* **1997**, *36*, 649.

(15) Hasegawa, Y.; Watanabe, K.; Kusakabe, K.; Morooka, S. *Sep. Purif. Technol.* **2001**, *22–23*, 319.

(16) Hasegawa, Y.; Watanabe, K.; Kusakabe, K.; Morooka, S. *J. Membr. Sci.* **2002**, *208*, 415.

(17) Gu, X.; Dong, J.; Nenoff, T. M. *Ind. Eng. Chem. Res.* **2005**, *44*, 937.

(18) Cheng, Z.; Gao, E.; Wan, H. *Chem. Commun.* **2004**, 1718.

(19) Guillou, F.; Rouleau, L.; Pirngruber, G.; Valtchev, V. *Microporous Mesoporous Mater.* **2009**, *119*, 1.

(20) Kumakiri, I.; Yamaguchi, T.; Nakao, S. *Ind. Eng. Chem. Res.* **1999**, *38*, 4682.

(21) Holmberg, B. A.; Wang, H.; Norbeck, J. M.; Yan, Y. *Microporous Mesoporous Mater.* **2003**, *59*, 13.

(22) Nair, S.; Tsapatsis, M. In *Handbook of Zeolite Science and Technology*; Auerbach, S. M., Carrado, K. A., Dutta, P. K., Eds.; Marcel Dekker: New York, 2003.

(23) Li, Q. H.; Creaser, D.; Sterte, J. *Chem. Mater.* **2002**, *14*, 1319.

(24) Mintova, S.; Olson, N. H.; Bein, T. *Angew. Chem., Int. Ed.* **1999**, *38*, 3201.

(25) Kuzniatsova, T. A.; Mottern, M. L.; Chiu, W. V.; Kim, Y.; Dutta, P. K.; Verweij, H. *Adv. Funct. Mater.* **2008**, *18*, 952.

(26) Hedlund, J.; Korelskiy, D.; Sandstrom, L.; Lindmark, J. *J. Membr. Sci.* **2009**, *345*, 276.

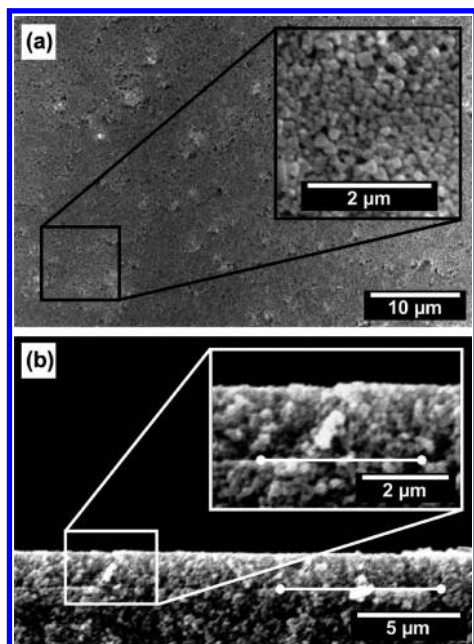


Figure 2. SEM image of (a) top view and (b) cross-section of submicrometer zeolite Y seed layer using 5 mg/mL zeolite concentration.

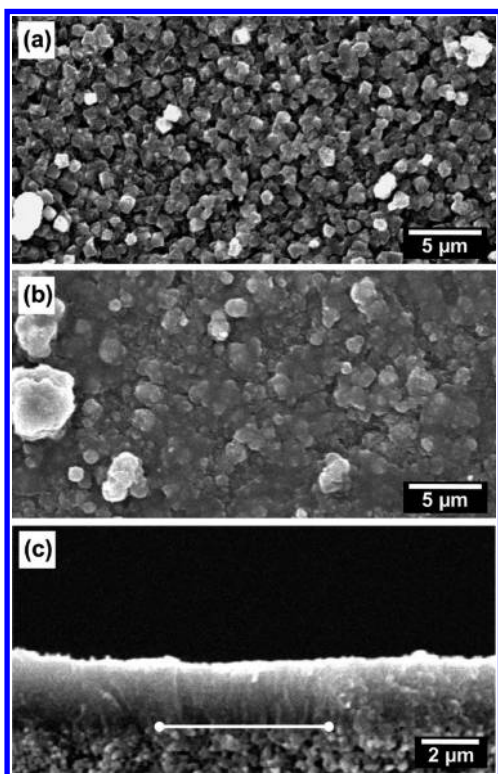


Figure 3. SEM images demonstrating the densification in a submicrometer zeolite Y membrane using composition A: (a) top view and (b) cross-section after 16 h growth.

ensuing membrane in Figure 3b suggests that membrane continuity had improved. The SEM cross-section in Figure 3c shows that membrane thickness is 2–2.5 μm after two consecutive secondary growth experiments. The XRD pattern shown in Figure 1c suggests the zeolite Y crystal structure.

Composition B results in slower growth of zeolite Y. During 7 days of growth at 373 K, the solution became turbid after 4 days,

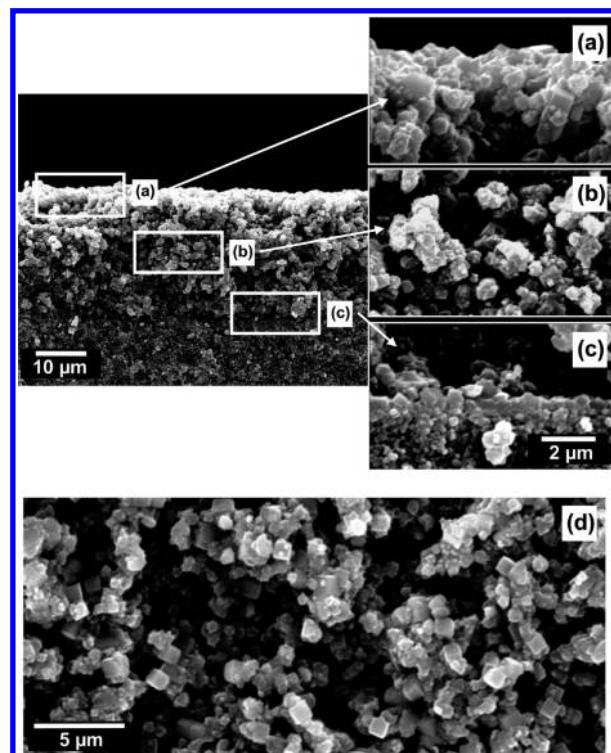


Figure 4. SEM images showing the submicrometer zeolite Y membrane microstructure using composition B. (a–c) Cross-section highlighted by three different regions after 7 days growth. (d) Top view after 7 days growth.

and a precipitate formed after the sixth day. SEM cross-sectional and top-view images of the composition B membrane are provided in Figure 4a–d. This shows that the cross-section is divided into three layers. The top and middle layer (a and b, respectively) were found to be porous with a combined thickness of 25 μm . However, as seen in part c, there is a dense layer directly present on the alumina support with a thickness varying between 350 and 600 nm. The SEM top-view in Figure 4d confirms the presence of the porous zeolite layer shown in Figure 4a–c. Powder XRD in Figure 1d showed that the membrane is primarily zeolite Y.

Further insight into the mechanism of the membrane formation in composition B was obtained in an experiment with smaller (25–50 nm) zeolite Y seeds. These nanocrystals were dispersed in aqueous 1.5 wt % polyethylenimine (PEI), with a concentration of 3.2 mg/mL. A representative seed layer formed by dip-coating is shown in Figure 5a, with a seed layer thickness of 350–375 nm. After secondary growth in composition B for 4 days, the SEM data shown in Figure 5b indicated that no membrane is formed on the alumina support, but instead, a random deposition of submicrometer zeolite Y and larger zeolite A crystallites. The SEM top-view in Figure 5c also indicates the incomplete formation of a membrane based on the still visible grains of the alumina support.

Gas Separation Properties. For each membrane type formed with compositions A and B (Figure 3c and 4c), 2–3 samples were analyzed by single gas permeation and gas separation measurements using the apparatus shown in Figure 6, with similar results. The data presented here is from the best performing membrane of each type. For the as-synthesized membranes that were water-saturated, no single gas CO_2 or N_2 permeation could be detected; however, permeation was observed after heating the membranes overnight at 423 K. The single gas permeance results are shown in Table 1; $f_{\text{CO}_2, \text{B}}^{\text{s}}$ was 25–40 times greater than $f_{\text{CO}_2, \text{A}}^{\text{s}}$; $f_{\text{N}_2}^{\text{s}}$ was similar for both membranes and near the detection limit.

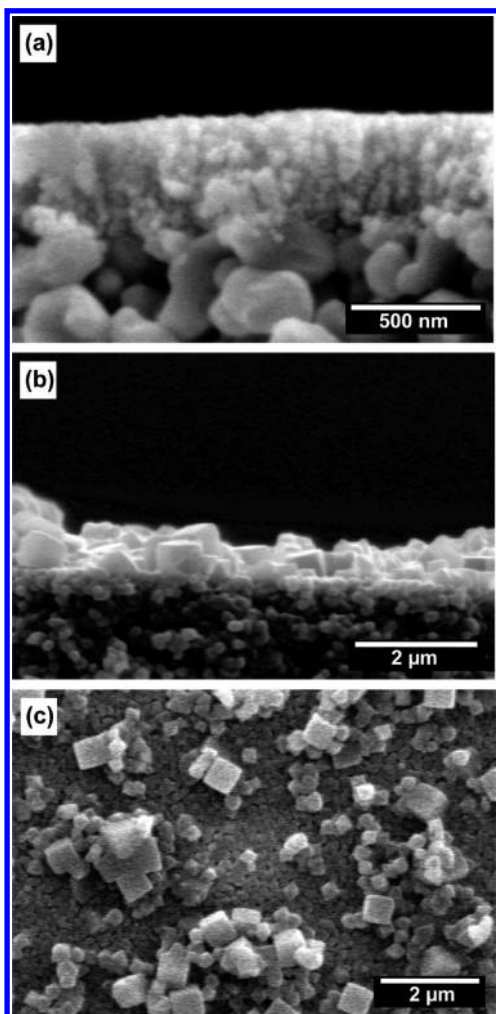


Figure 5. SEM images emphasizing the nanocrystalline zeolite Y seed layer and lack of membrane formation using composition B: (a) cross-section of seed layer formed using a 3.2 mg/mL zeolite concentration; (b) cross-section after 4 days growth; (c) top-view after 4 days growth.

For membrane B, permselectivities ($\alpha_{\text{CO}_2, \text{N}_2}^{\text{S}}$) of 18–30, were obtained. The permselectivities for membrane A were very high but their exact value could not be determined due to detection limitations for $f_{\text{N}_2, \text{A}}^{\text{S}}$.

The CO_2 permeability (k) for composition A membranes, having thicknesses of 2–2.5 μm , was established to be $(0.8\text{--}1) \times 10^{-14}$ mol/(m s Pa) at 303 K. At the same temperature, the CO_2 permeability for composition B membranes (350–600 nm thick, ignoring the top porous layer) was determined to be $(3\text{--}6) \times 10^{-14}$ mol/(m s Pa). Because of the fact that only one feed pressure was utilized for these single gas measurements, no pressure dependent data is reported.

Prior to the mixed gas separation experiments, the membranes were heated to 423 K. The actual measurements were carried out at temperatures of 303–403 K at a feed pressure of 207 and 138 kPa for membrane A and B, respectively. The $\alpha_{\text{CO}_2, \text{N}_2}$ data are summarized in Table 2; for composition B membranes, $\alpha_{\text{CO}_2, \text{N}_2}$ decreases with T , which has been previously demonstrated.^{8–10,14} Such an effect could not be established for composition A membranes since at all temperatures, $\alpha_{\text{CO}_2, \text{N}_2} > 550$. Membrane B showed the highest $\alpha_{\text{CO}_2, \text{N}_2} > 500$ at $T = 303$ K, and even at $T = 403$ K, $\alpha_{\text{CO}_2, \text{N}_2} > 40$ was observed.

The concentration and decomposition of intrazeolitic TMA in composition B membranes upon heating was examined to

establish its fate upon treatment at 423 K prior to the separation measurements. Figures 7a-b show infrared spectra collected on TMA-containing zeolite Y powder at temperatures ranging from 298 to 423 K for varying times. The bands below 1200 cm^{-1} arise from the zeolite. Even after 2 h at 423 K, minimal changes in intensities were observed for the bands corresponding to the TMA cations at 1405 (combination mode $951 + 457\text{ cm}^{-1}$), 1422 (CH_3 umbrella bending), 1488 (CH_3 asymmetric bending) and 3013 cm^{-1} (CH_3 asymmetric stretch) cm^{-1} ,²⁷ though the bands due to water at 1635 and 3400 cm^{-1} show a significant decrease. Elemental analysis on zeolite seed powders showed a carbon to nitrogen ratio (C/N) of 3.9 in untreated TMA-containing zeolite Y. That ratio remained the same after heating at 423 K for 4 days in flowing N_2 . Thus, both the IR and elemental analysis confirm that TMA undergoes minimal decomposition when the zeolite was heated up to 423 K for extended periods of time. Therefore, it was concluded that the TMA was still present in membranes B during the gas separation experiments. The C, N analysis also suggests a loading of 24 TMA molecules per unit cell. Assuming that all TMA molecules are in the supercage, TMA occupies $\sim 25\%$ of the supercage volume based on a TMA size of 0.66 nm.

Discussion

Membrane Formation. For membranes made from Composition B, two sets of seed crystals were examined, and the SEM images are shown in Figures 4 and 5. With nanozeolite Y as seeds, no membrane was formed (Figure 5b,c). Since the reaction vessel was not agitated or stirred during secondary growth, the zeolite seed crystals were not being physically lodged from the support surface. This leads us to conclude that zeolite dissolution is occurring during the secondary growth process. With the submicrometer zeolite Y seed crystals, (Figure 4), dissolution does still occur, but probably not as rapidly and to full completion as is the case for higher surface/volume ratio nanocrystals. Such dissolution phenomena has been also observed for zeolite A, TS-1, MFI, and ZSM-5.^{28–31} For both nano and submicrometer seeds used in synthesis of composition B membranes, dissolution of the seed crystals occurs in the initial stage. In the case of the submicrometer seed layer, partial dissolution is followed by secondary growth of the remaining zeolite Y nuclei at the alumina interface. The thick 25 μm porous zeolite layer is likely formed from secondary nuclei that are generated further away from the surface at lower concentrations. In contrast, the growth of composition A membrane occurs in a much shorter time by rapid intergrowth within the seed layer. This does not allow the seed crystals enough time to dissolve before being converted into a dense membrane. Efforts were made to vary the growth times and sample orientation to get rid of the thick porous layer in composition B membranes, but these led to discontinuous membranes and defects.

Membrane Transport. Although the eventual membrane types are considerably different in their membrane microstructure and morphology, the CO_2 transport properties are quite similar when the membrane thickness is taken into consideration (the porous layer in composition B membrane (Figure 4a) is not

(27) Spinner, E. *Spectrochim. Acta, Part A* **2003**, *59*, 1441.

(28) Matsukata, M.; Sawamura, K.; Shirai, T.; Takada, M.; Sekine, Y.; Kikuchi, E. *J. Membr. Sci.* **2008**, *316*, 18.

(29) Uemiyama, S.; Tanigawa, A.; Koike, T.; Sasaki, Y.; Ban, T.; Ohya, Y.; Yoshiie, R.; Nishimura, M.; Yamamoto, N.; Yogo, K.; Yamada, K. *J. Porous Mater.* **2007**, *15*, 405.

(30) Qiu, F.; Wanga, X.; Zhanga, X.; Liua, H.; Liua, S.; Yeungb, K. L. *Chem. Eng. J.* **2009**, *147*, 316.

(31) Li, S.; Li, Z.; Bozhilov, K. N.; Chen, Z.; Yan, Y. *J. Am. Chem. Soc.* **2004**, *126*, 10732.

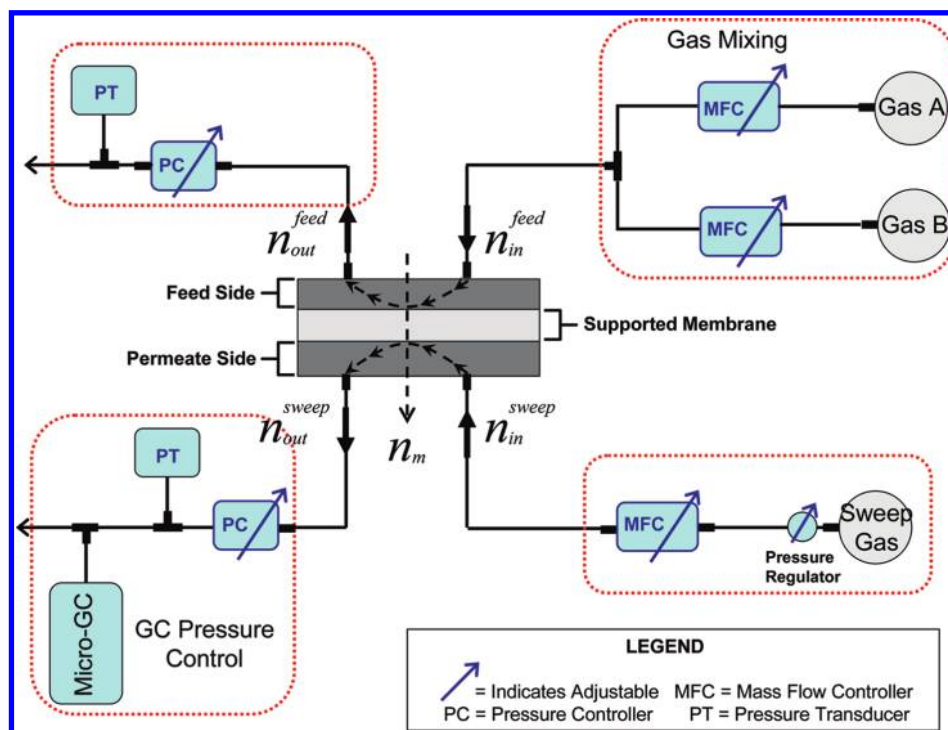


Figure 6. Diagram of the mixed gas separation setup.

Table 1. Summary of the Single Gas Permeances (f^s) for CO₂ and N₂ at 207 kPa, as Well as the Permselectivities ($\alpha_{\text{CO}_2, \text{N}_2}^s$) and CO₂ Permeabilities (k) for Composition A and B Membranes

test temperature (K)	composition A membranes				composition B membranes			
	permeance (mol/m ² s Pa)		$\alpha_{\text{CO}_2, \text{N}_2}^s$	CO ₂ permeability (mol/m s Pa) ^a	permeance (mol/m ² s Pa)		$\alpha_{\text{CO}_2, \text{N}_2}^s$	CO ₂ permeability (mol/m s Pa) ^b
CO ₂	N ₂	CO ₂			N ₂			
403	4.1×10^{-9}	$< 3.0 \times 10^{-9}$	ND	$(0.8-1) \times 10^{-14}$	1.1×10^{-7}	4.4×10^{-9}	25.0	$(3-6) \times 10^{-14}$
353	3.3×10^{-9}	$< 3.0 \times 10^{-9}$	ND		1.3×10^{-7}	4.4×10^{-9}	29.5	
303	3.9×10^{-9}	$< 3.0 \times 10^{-9}$	ND		9.6×10^{-8}	5.1×10^{-9}	18.8	

^a Membranes with thicknesses ranging from 2 to 2.5 μm . ^b Membranes with thicknesses ranging from 0.35 to 0.6 μm .

contributing to the separation; this layer just acts to build up a thick stationary layer of the gases and possibly influences the separation negatively). On the other hand, the N₂ permeability of membrane A is 1 order of magnitude less than that of membrane B. Different gas transport mechanisms for the two gases can explain these observations. For CO₂, transport through the membrane is thought to occur by an activated surface diffusion mechanism.¹⁰ For nitrogen, the mechanism is considered to be primarily ballistic.

Nonstationary single gas permeation experiments on defective and noncontinuous membranes showed f^s approaching the support permeance (10^{-7} mol/(m² s Pa)). For the as-grown membranes presented here, no detectable CO₂ or N₂ was observed at a feed pressure of 207 kPa after 24 h, which confirms that the membranes were fully continuous. Removal of the intrazeolitic water by heat treatment resulted in the membrane transport properties shown in Table 1. Composition B membranes had a CO₂ flux that was higher by an order of magnitude or more as compared to composition A membranes. The permselectivities for membrane B already indicate very high intrinsic selectivities, as shown in Table 1. The CO₂ permeance of membrane B (1×10^{-7} mol/(m² s Pa)) approached that of the bare alumina support ($(3-4) \times 10^{-7}$ mol/(m² s Pa)).

The temperature effect on the CO₂/N₂ selectivity for membranes A and B is consistent with previous reports, in which the highest selectivities were obtained at temperatures < 323 K.^{8-10,14}

Table 2. Summary of $\alpha_{\text{CO}_2, \text{N}_2}$ for Composition A and B Membranes at Various Temperatures (Retentate Feed Pressures Are Noted in Table)

test temperature (K)	composition A membranes	composition B membranes
	$\alpha_{\text{CO}_2, \text{N}_2}$ for retentate pressure	
	207 kPa	138 kPa
303	> 550	503
353	> 550	94
403	> 550	41

The relation between $\alpha_{\text{CO}_2, \text{N}_2}$ and $\alpha_{\text{CO}_2, \text{N}_2}^s$ depends on the average occupation, $0 < \theta < 1$, of the micropores in the membrane.¹³ For the proposed membranes and conditions, $\theta_{\text{CO}_2} > 0.5$ and $\theta_{\text{N}_2} < 0.1$ so that $\alpha_{\text{CO}_2, \text{N}_2} \gg \alpha_{\text{CO}_2, \text{N}_2}^s$ in what was previously described as type II separation. The data presented for membrane B in Tables 1 and 2 show strong evidence for type II separation based on the fact that $\alpha_{\text{CO}_2, \text{N}_2}$ is much higher than $\alpha_{\text{CO}_2, \text{N}_2}^s$ determined from the single gas permeances. The differences between $\alpha_{\text{CO}_2, \text{N}_2}$ and $\alpha_{\text{CO}_2, \text{N}_2}^s$ at temperatures ≤ 353 K are even more significant (> 60) when compared to the experimental values at 403 K.

Comparison to Literature. Table 3 shows a comparison between permeance and selectivity of the zeolite Y membranes in this study with those reported in the literature. The membranes in Table 3 have different support types, Si/Al ratios, as well as

thickness (0.7–60 μm), all of which can greatly affect the overall membrane performance. At temperatures below 323 K, the

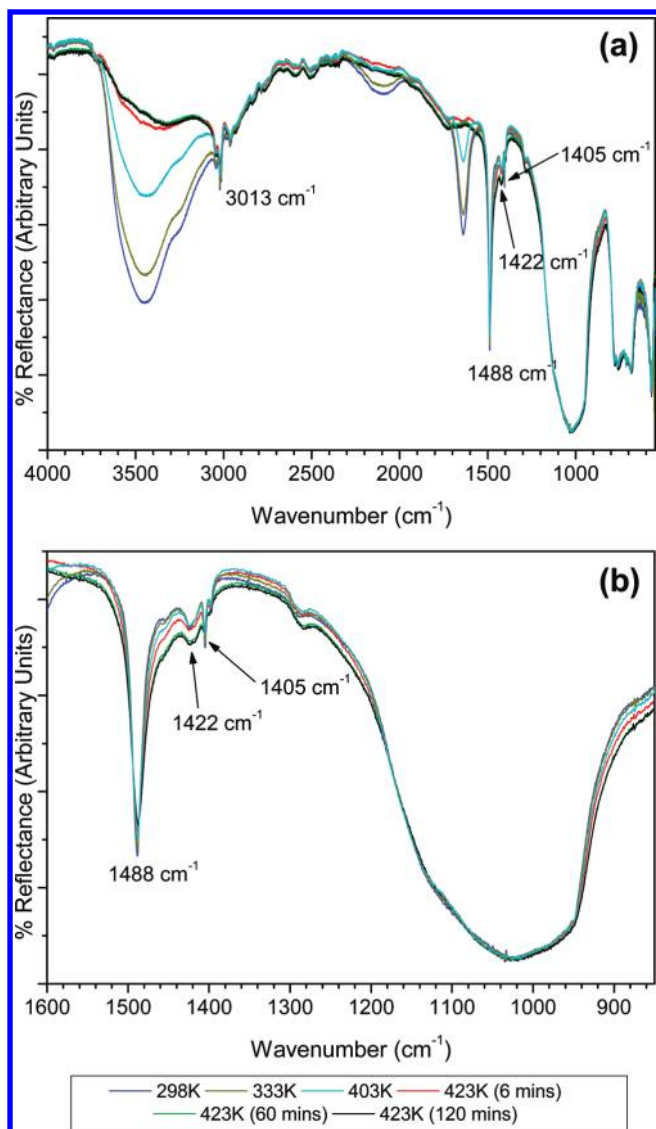


Figure 7. DRIFTS spectra monitoring the in situ decomposition of TMA in submicrometer zeolite Y at 423 K.

reported CO_2 permeances are $(1.5\text{--}5) \times 10^{-7} \text{ mol}/(\text{m}^2 \text{ s Pa})$, with $\alpha_{\text{CO}_2/\text{N}_2} = 6\text{--}54$. The single most selective membrane ($\alpha_{\text{CO}_2/\text{N}_2} \sim 100$ at 303 K) in Table 3 is approximately 10 μm thick and has a f_{CO_2} of $(2\text{--}3) \times 10^{-8} \text{ mol}/(\text{m}^2 \text{ s Pa})$.²³ The least selective membrane in Table 3 has a $\alpha_{\text{CO}_2/\text{N}_2} = 6$ at 323 K with thickness $< 1 \mu\text{m}$ thick, and a permeance of $3.5 \times 10^{-7} \text{ mol}/(\text{m}^2 \text{ s Pa})$.

The $\alpha_{\text{CO}_2/\text{N}_2}$ of membrane A (> 550) far exceeds that for any existing zeolite Y membrane below 323 K. Even at 403 K, membrane A was found to have a higher selectivity than those reported earlier at lower temperatures. However, the $f_{\text{CO}_2/\text{A}}$ of composition A membranes is 20–200 \times less than that of the published membranes.

Membrane B also has better CO_2/N_2 separation performance when compared to the membranes in Table 3, with selectivities as high as 500. Although the selectivity decreases with increasing temperature for membrane B, $\alpha_{\text{CO}_2/\text{N}_2}$ is still > 40 at 403 K, with CO_2 permeances similar to the published membranes. These results show the versatility of using membrane B over a wide range of experimental temperatures, based on the fact that the separation between CO_2 and N_2 typically diminishes above 353 K for zeolite Y membranes, as shown in Table 3.

However, when comparing composition B membrane to those in Table 3, there are several reported membranes that are more permeable to CO_2 (2–15 times). Those membranes that had $f_{\text{CO}_2} < 1 \times 10^{-7} \text{ mol}/(\text{m}^2 \text{ s Pa})$ at $< 323 \text{ K}$, were reported as having $\alpha_{\text{CO}_2/\text{N}_2} < 35$. Membrane B demonstrates better selectivities (> 500), but lower permeances. For those membranes in Table 3 that have a $\alpha_{\text{CO}_2/\text{N}_2} > 35$, the CO_2 permeances are either the same or less than those for the membrane B.

Conclusions

Submicrometer zeolite Y seeds were dip-coated onto macroporous alumina supports and grown into homogeneous, dense membranes. Two different secondary growth solutions were utilized, with fast (composition A) and slow growth (composition B) characteristics. The rapid growth procedure led to uniform zeolite membranes of 2 μm thickness, with very high selectivity for CO_2 separation from N_2 , but with low permeance. The slower growth procedure resulted in membranes that were 25 μm thick, with most of the membrane being highly porous, in addition to a dense 350–600 nm thick continuous membrane on the support. This thin layer determined the overall transport properties, which resulted in a substantially higher permeance and may be of practical use in fabricating membranes capable of separating CO_2 from N_2 and

Table 3. Comparison of Published Reported Performances of FAU-Type Membranes in CO_2/N_2 Separations versus Membranes in This Study^a

ref	membrane area (cm^2)	support type/shape	membrane thickness (μm)	retentate feed pressure (kPa)	test temperature (K)	permeance ($10^{-7} \text{ mol}/\text{m}^2 \text{ s Pa}$)		
						CO_2	N_2	$\alpha_{\text{CO}_2/\text{N}_2}$
14	17.6	α -alumina tube	10	101	303	0.28 ^c	0.1	100 ^c
8	17.6	α -alumina tube	10	101	313	4.1 ^b	0.09	46 ^b
10	17.6	α -alumina tube	10	101	308	13 ^b	0.44	30 ^b
9	0.8	α -alumina tube	5	101	308	15 ^b	0.47	32 ^b
16	13.2	α -alumina tube	3	101	308	11 ^b	0.3	37 ^b
17	6.6	α -alumina disk	4	86	323	0.39 ^b	0.02	20 ^b
19	24	α -alumina tube	10	130	323	3.48 ^c	0.28	5.7 ^c
	24	α -alumina tube	10	130	343	3.58 ^c	0.46	4.2 ^c
15	13.2	α -alumina tube	3	101	308	8.6 ^b	0.45	19 ^b
7	1	peeled from SS plate	60	101	298	5.4 ^b	0.27	20 ^b
18	4.5	α -alumina disk	50	298	298	1.5 ^b	0.028	54 ^b
	4.5	α -alumina disk	50	373	373	2.0 ^b	0.08	25 ^b
membrane A	7	α -alumina disk	1.9–2.1	207	303	0.039 ^c	0.029	> 550 ^c
membrane A	7	α -alumina disk	1.9–2.1	207	403	0.041 ^c	0.03	> 550 ^c
membrane B	7	α -alumina disk	0.35–0.6	138	303	0.96 ^c	0.051	503 ^c
membrane B	7	α -alumina disk	0.35–0.6	138	403	1.1 ^c	0.044	41 ^c

^a For all experiments, the permeate pressure was maintained at atmospheric pressure. ^b Permeances and selectivity determined from mixed gas separation experiments. ^c Permeances determined by single gas permeation experiments; selectivity determined from mixed gas separation experiments.

other gases over a wider range of temperatures and pressures. Membranes could not be formed when starting from nanometer sized seeds. Hence, we concluded that dissolution of seed crystals is an important step in membrane growth with composition B. On the basis of these results, our ongoing research will be focused on strategies to prepare highly permeable dense ultrathin zeolite Y membranes without the porous layer.

Acknowledgment. This work was supported by The Basic Research for the Hydrogen Fuel Initiative Program (DOE, Grant No. DF-FG01-04FR04-20).

Supporting Information Available: Text giving the experimental section. This material is available free of charge via the Internet at <http://pubs.acs.org>.